UNIVERSITY OF TWENTE.

Bachelor thesis

Possible enhancement of thermoelectric p-type oxides by creating superlattice structures with pulsed laser deposition

Faculty of Science and Technology
Inorganic Materials Science

Author:
Chris Nawrath

Bachelor commission:
Dr. Ir. Mark Huijben
Ir. Peter Brinks
Prof. Dr. Guido Mul

December 6, 2013

Abstract

Advanced thermoelectric materials are part of considerations about the future energy handling. They promise to be a direct and easy method to convert waste heat into easy usable electrical energy. General problem in optimizing thermoelectric properties seems to be the coupled behavior of electrical and thermal properties. Superlattice structures are a promising approach to lower thermal transport and at the same time to preserve the electrical conductivity.

In this work 3 superlattices of the thermoelectric oxides Na_xCoO_2 and $Ca_3Co_4O_9$ are prepared by pulsed laser deposition on top of $[La_{0.3}Sr_{0.7}][Al_{0.65}Ta_{0.35}]O_3$ (LSAT) substrates. X-ray diffraction (XRD) scans and resistivity measurements are done of the samples and the Seebeck coefficients are determined. Furthermore it is theoretically considered how thermal properties can be affected by superlattice structures.

XRD measurements showed, that $Ca_3Co_4O_9$ tends not to grow crystalline under the used deposition temperatures (430°C). Therefore a reference sample is used of $Ca_3Co_4O_9$ on top of a thin layer of Na_xCoO_2. All samples showed similar crystallographic ordering and the peak around 16° was used to look at the differences in detail. All superlattices showed interplanar distances in between the two reference samples and in sequence of the total thickness ratio of both components. Shape and height of the peaks showed, that Na_xCoO_2 still seemed to grow more crystalline than $Ca_3Co_4O_9$.

The measured Seebeck coefficient of the Na_xCoO_2 thin layer was as expected $79 \pm 3\ \mu V/K$ and the one of the $Ca_3Co_4O_9$ reference sample with 136 ± 7 $\mu V/K$ lower than other reported values. The superlattices were all in between those two values, showing a *mixed* Seebeck coefficient. That indicates, that the Seebeck coefficient is not influenced by the superlattice structure in particular.

All samples containing both materials, Na_xCoO_2 as well as $Ca_3Co_4O_9$, showed rising resistivities, suggesting a reaction occurring. They did not get stable in the course of the entire bachelor project. Furthermore a change in color was observed spreading from the edges of the samples. Either there is a new undiscovered reaction occurring between the two materials or the earlier found reactions between Na_xCoO_2 and air (possibly achieving the sample from the edges or through an insufficient capping layer) appear again.

Theoretical calculations showed that it would be favorable to compose superlattices with smaller thicknesses of the single layers than done in this work. Worse properties were reported for thin films with layers thinner than approx. 10 nm. However the superlattices seem not to suffer from this problem.

Contents

1 Introduction

Energy production and environmental issues are two of the most discussed topics nowadays. In the future energy has to be used and produced more sustainable and effective to avoid supply shortage and to preserve the environment. A huge amount of energy is still lost as waste heat to the surroundings. One possibility to collect this energy and reuse it is to apply materials with thermoelectric (TE) effects. In thermoelectric materials a voltage is induced between two sides if the sides are held at different temperatures [1, Ch.1]. TE materials are known for a long time and are used since the 70s for some special applications, such as spot cooling of electronics or power generating for deep space probes and other remote systems [2]. In comparison with other thermodynamic heat-to-electricity conversion processes (e.g. stirling engine + electric generator), TE materials are easier to apply in every scale and more reliable, because of the absence of moving parts [2]. But on the other hand they are also often more expensive and in most cases still less effective. Furthermore the most commonly used materials are toxic and not suitable for high-temperature applications due to stability issues [2]. These materials have been investigated for a long time and large improvements are not expected anymore.

To have good thermoelectric properties a material needs to have a poor thermal and good electrical conductance as well as a large Seebeck coefficient – the entropy per charge carrier, a basic material property [1]. There are several classes of new materials which provide interesting TE properties, too, but they are not investigated enough yet [2]. One of these classes is the class of TE oxides. Oxides were expected to have poor TE properties, because of their unfavorable structure containing atoms with high electronegativities leading to low electrical conduction and a high symmetry resulting in a high thermal conduction [2]. But nevertheless the TE properties were surprisingly good [3] which indicates a new possible way of manipulating them. In general oxides are well known and have good chemical stability at high temperatures.

Aim of this thesis is to research the possibility to enhance the properties of thermoelectric oxides by creating superlattices of different TE oxides by pulsed laser deposition (PLD). As earlier mentioned, improvement of TE properties will be achieved, if the thermal conductivity can be decreased while the electric properties are not harmed. The electronic and structural properties of superlattices consisting of Na_xCoO_2 and $Ca_3Co_4O_9$ and the effects of variations in the layer thicknesses will be studied. The superlattices are produced by PLD which provides sufficient control on the growth process. There are some theoretical considerations given about affecting thermal transport in superlattices in this work, too.

2 Background information

2.1 Thermoelectric parameters

To find appropriate chemical compounds for thermoelectric applications one has to define the important parameters that affect the efficiency. The efficiency (Φ) for a thermoelectric power generating device can be expressed in the form of Equation 1 with T_H and T_C respectively the absolute temperature of the hot and the cold side [1, Ch. 1]. The first bracketed term in this equation is the so called Carnot efficiency[a] and the rest of the equation is maximized by a high value of ZT. ZT is called the dimensionless figure-of-merit and given in Equation 2 with α the Seebeck coefficient, T the average temperature, κ the thermal conductivity and ρ the electrical resistivity. The Seebeck coefficient α is the voltage over a thermoelectric element divided by the temperature difference ($U/\Delta T$) and can be seen as the mean entropy per charge carrier [2]. The figure-of-merit (ZT) is the value on which materials are most times compared. In some cases the power factor PF (see Equation 3) is used instead, which does not include the thermal conductivity and average temperature.

$$\Phi = \left(\frac{T_H - T_C}{T_H}\right)\frac{\sqrt{1+ZT}-1}{\sqrt{1+ZT}+\frac{T_C}{T_H}} \tag{1}$$

$$ZT = \frac{\alpha^2 T}{\kappa\rho} \tag{2}$$

$$PF = \frac{\alpha^2}{\rho} \tag{3}$$

The thermal resistivity ρ and the Seebeck coefficient α both depend on the charge carrier concentration of a material. A high charge carrier concentration leads to a good electrical conductivity (and thus to a low resistivity), but also to a lower entropy per charge carrier. Therefore ZT has a maximum around a charge carrier concentration of $10^{19} cm^{-3}$ [1, Ch. 1] which corresponds to semiconducting materials. Since the 1970s the most used and studied materials are Bi_2Te_3 (maximum ZT of 1 at 400 K) and $Si_{1-x}Ge_x$ (maximum ZT of 1 at 1200 K) [2]. Thermoelectric devices consist most times of two different types of semiconductors – a p-type material with more free positive charge carriers and an n-type material with more free electrons. Although there are some n-type candidates, this thesis concentrates on thermoelectric p-type oxides.

[a] The Carnot efficiency is the maximum efficiency given by thermodynamics

2.2 Sodium cobalt oxide

A big step forward in the research on thermoelectric oxides was the discovery of the thermoelectric properties of Na_xCoO_2 by Terasaki et al. in 1997 [3]. They prepared single crystals with the composition $Na_{0.5}CoO_2$ by a NaCl-flux technique. The obtained crystals had a quasi-2-dimensional structure consisting of alternating layers of Na and CoO_2. The CoO_2 layer consists of distorted oxygen octahedra with cobalt ions at the center [1, Ch. 35]. There are vacancies at the oxygen positions and furthermore the sodium ions are positioned randomly in the center of the prism sites between the CoO_2 layers. This structure is highly anisotropic and the Seebeck coefficient and the electrical resistivity measured in the in-plane direction are respectively 200 $\mu\Omega cm$ and 100 $\mu V/K$ leading to a power factor of 50 $\mu W/(K^2cm)$ which is comparable to the power factor of Bi_2Te_3 (40 $\mu W/(K^2cm)$) [3]. This result was not expected, because $Na_{0.5}CoO_2$ has a much lower charge carrier mobility ($\mu_{Na_{0.5}CoO_2} = 13cm^2/Vs \ll \mu_(Bi_2Te_3) = 150cm^2/Vs$ [3]) which was supposed to cause a lower electrical conductance and a lower Seebeck coefficient. This study implied that there needs to be another mechanism besides the already known one that affects thermoelectric properties. The results got a lot of attendance and the field of thermoelectric oxides was rising quickly and other materials with similar properties were found.

Polycrystalline samples were produced by a solid-state reaction from Na_2Co_3 and Co_3O_4 [4]. In addition to the electric properties the thermal properties were measured of these samples and single crystalline samples at different temperatures [4]. The results of the measurements at 300 K and 800 K are displayed in Table 1 after section 2.4. At higher temperatures the electrical resistivity and the Seebeck coefficient rises and the thermal conductivity decreases. These are general trends and lead to a significant higher figure-of-merit. At 800 K a single crystalline sample of Na_xCoO_2 reaches a ZT of 1.2 which exceeds the ZT of the conventional $Si_{0.95}Ge_{0.05}$ by far. The increase in electrical and thermal resistivities with increasing temperature can be explained by the higher scattering of phonons and electrons at high temperatures. The higher electric resistivity of polycrystalline samples compared with single crystalline ones can be explained by electron scattering at the interfaces and a higher resistivity in the out-of-plane direction due to the crystal structure [4]. The lower thermal conductivity of polycrystalline samples is more likely to be caused by the fact that a preferred path with high conductivity through the ab-planes is not present than by influences of the interfaces, because the mean free path of phonons is closer to the c-axis lattice parameter (10.9 $\AA$) than to the grain size ($\sim 10\mu m$) [4].

In polycrystalline samples of Na_xCoO_2 that were produced by solid-state reactions with different stoichiometric amounts of sodium (ranging from

0.48 to 0.76) a minimum in the electrical resistivity was observed at the ratio $Na_{0.68}CoO_2$ [5]. Furthermore there is a jump detected in $d\rho/dT$ for every substance at a temperature T_x depending on the amount of sodium. The minimum T_x is again found by $x = 0.68$ [5].

2.3 Calcium cobalt oxide

Based on the Na_xCoO_2-structure there are several other cobaltite materials that have the alternating layered structure in common with CoO_2 as one of the layers. One of these materials is calcium cobalt oxide ($Ca_3Co_4O_9$). It is also sometimes denoted by $[Ca_2CoO_3]_{0.62}[CoO_2]$ [6]. Besides the CoO_2 layer the other Ca_2CoO_3 layer has a rock-salt type crystal structure. There is a misfit between both layers due to the different types of crystal structure and the different interatomic distances. That induces phonon-phonon interactions resulting in a lower thermal conductivity [7]. Measurements of single crystals grown by a modified strontium chloride flux technique are given in Table 1, too.

Textured samples of $Ca_3Co_4O_9$ are obtained by a chemical co-precipitation method followed by spark plasma sintering [8]. Properties of these samples at 700°C are displayed in Table 1 as well. Another possibility to improve the thermoelectric properties of polycrystalline samples of $Ca_3Co_4O_9$ is to apply a high magnetic field during sintering to align the grains along the c-axis and forward the anisotropy so that the undesired properties in the out-of-plane direction get less impact [9]. Measurements of samples produced by this method under a magnetic field of 8T are included to Table 1.

2.4 Thin films and superlattice approach

As can be seen by the conventional approaches to obtain a higher ZT, boundaries seem to play an important role. On the one hand they have an effect on electronic transport making in general single crystals better electrical conducting than polycrystalline samples. On the other hand polycrystalline materials have a lower thermal conductivity, which is desired, too. The layer misfit in $Ca_3Co_4O_9$-structures is not a real boundary, but has an effect on the thermal conductivity due to phonon-phonon interactions.

There are three basic approaches to enhance thermoelectric properties by thin film techniques [10]. One approach is, as mentioned before, to create superlattice structures that reduce phononic transport and/or enhance electronic transport. It is theoretically predicted that there is a minimum in the thermal conductivity in the out-of plane direction at a layer thickness a little bit smaller than the mean free path of the phonons [11]. This is already proven for superlattices consisting of Si−Ge [12]. Epitaxial Si−Ge

superlattices have the same electrical conductivity as Si−Ge bulk alloys but indeed a lower thermal conductivity. At smaller periods the thermal conductivity decreases with decreasing period lengths due to the absolutely larger amount of Si−Ge interfaces that lower the phonon transport as predicted. At longer periods there is another low thermal conductivity behavior found that is put down to a rise in defect concentrations due to a high epitaxial strain [12].
A second approach is to use quantum-confinement effects to control the energy levels of the charge carriers [10]. By doing so it is possible to adjust the energy levels to give more electrons near the Fermi energy. This obtains a higher amount of free charge carriers for electronic conduction and a better conductivity. The theoretical potential of this approach is calculated based on Bi_2Te_3 and there is a possible increase of ZT by a factor between 3 and 13 predicted [13]. Improvement of the figure-of-merit with this approach is obtained in $PbSe_xTe_{1-x}$/PbTe quantum-dot superlattices produced by molecular beam epitaxy (MBE) [14]. The obtained figures of merit are approximately two times the best bulk PbTe values.
The last approach is to produce structures that show thermionic effects [10]. Thermionic effects are actually not part of thermoelectric effects, but are similar to those in some manner. Thermionic cooling appears if an electron with high energy escapes over an energy barrier [15]. To prevent the reverse situation an electric field can be applied. The length of the layer needs to be smaller than the mean free path of the electron in order to create such a desired barrier from a semiconductor. Since these small layers are also only a low barrier against thermal conduction the obtained temperature differences between the layers need to be small and hence there is a multilayer structure with many layers needed for reasonable cooling effects [15].

Stability issues have been detected in thin film samples of Na_xCoO_2 produced by pulsed laser deposition [16]. These stability issues arise due to a reaction of the sodium with moisture and carbon dioxide from the air at the surface and can be prevented by adding *in situ* an amorphous AlO_x capping layer [17]. Measurements of thin films of Na_xCoO_2 with AlO_x capping layer grown on Al_2O_3 and $LaAlO_3$ are also added to Table 1.

$Ca_3Co_4O_9$ is produced by PLD, too. At high deposition rates the unsaturated phase Ca_xCoO_2 can be observed [18]. Calcium cobalt oxide seems to grow strain-free on several substrates[b] while having a Ca_2CoO_3 buffer layer between the thin layer and the substrate [19]. In general defects seem to have more influence on the material properties than epitaxial strain [19].

[b] $SrTiO_3$, $LaAlO_3$, $La_{0.3}Sr_{0.7}Al_{0.65}Ta_{0.35}O_3$ (LSAT) and AL_2O_3 [19]

Table 1: Comparison of data from literature. The temperature (T), the electrical resistivity (ρ), the Seebeck coefficient (α), the power factor (PF), the thermal conductivity (κ) and the dimensionless figure of merit (ZT). The measured properties of the samples are in the in-plane direction. Bi_2Te_3 and $Si_{0.95}Ge_{0.05}$ are the commonly used conventional materials.

	Terasaki et al.[3]		Fujita et al.[4]						Shikano et al.[7]	Zhang et al.[8]
	Na_xCoO_2 single crystal	Bi_2Te_3 bulk	Na_xCoO_2 single crystal		Na_xCoO_2 polycrystalline		$Si_{0.95}Ge_{0.05}$ bulk		$Ca_3Co_4O_9$ single crystal	$Ca_3Co_4O_9$ textured
T[K]	300	300	300	800	300	800	300	800	973	973
ρ[mΩcm]	0.2	1	0.3	0.5	2	3.6	0.8	1.7	2.3	9.3
α[μV/K]	100	200	83	200	100	170	200	338	240	178
PF[μW/K^{2}cm]	50	40	23.8	76.9	5	8.1	52	67	-	-
κ[W/mK]	-	-	19	5.1	2	2.1	10	9.5	3	1.6
ZT[$-$]	-	-	0.03	1.2	0.08	0.31	0.16	0.57	0.87	0.21

	Huang et al.[9]	Brinks et al.[17]		Sun et al.[18]
	$Ca_3Co_4O_9$ textured	Na_xCoO_2 thin film on Al_2O_3	Na_xCoO_2 thin film on $LaAlO_3$	$Ca_3Co_4O_9$ thin film on Al_2O_3
T[K]	300	300	300	973
ρ[mΩcm]	2.5	0.8	1	9.4
α[μV/K]	177.7	45	69	240
PF[μW/K^{2}cm]	1.3	2.6	4.8	-
κ[W/mK]	1.9	4	4	-
ZT[$-$]	0.02	0.01	0.03	-

3 Theory

An idea to lower the lattice thermal conductivity is to build superlattices affecting the wavelengths of phonons. Therefore there has to be some interaction in the same range of the wavelengths. In the next subsection 3.1 a formula is given to determine these wavelengths. It is possible to calculate the cutoff wavelength λ_{10}, where 10% of all wavelengths are smaller than λ_{10} and in a similar manner λ_{90}. After this phonon wavelengths practically obtained from Raman spectroscopy and considerations about the mean free path of phonons are discussed.

3.1 Calculation of phonon wavelength range

The range of wavelengths of phonons present in a material can be expressed in terms of the smallest allowed wavelength λ_0:

$$\lambda_0 = \frac{2\pi}{\sqrt[3]{6\pi^2 N}} \tag{4}$$

Herein is N the number density of unit cells which can be calculated from the dimensions of the unit cells [1, Ch. 42]. Furthermore is the phonon spectrum dependent on the Debye temperature T_0 of the material [1, Ch. 42]:

$$T_0 = \frac{h v_s}{k_B \lambda_0} \tag{5}$$

with h = Planck's constant, v_s = velocity of sound and k_B = Boltzmann's constant. Well below the Debye temperature the phonon behavior can be summarized by the following expression:

$$\lambda_\alpha T = \gamma_\alpha \left(\frac{v_s}{5000 \frac{m}{s}} \right) \tag{6}$$

α is the percentage of phonons that have a smaller wavelength than λ_α and there are several values for the parameter γ_α given for different weightings [1, Ch. 42]. At higher temperatures than T_0 the ratio $\frac{\lambda_\alpha}{\lambda_0}$ tends to be constant and is also given [1, Ch. 42].

The calculated values for the number density of unit cells and the smallest allowed wavelength of phonons is given in the table below. For calcium cobalt oxide both calculations corresponded to the different lattice b axis parameters are done[c] and given in Table 2 below.

The velocities of sound inside the materials are needed, too, in order too calculate the Debye temperature. They could not be found directly in

[c] As earlier discussed consists calcium cobalt oxide of different layers with a layer mismatch between them.

Table 2: Lattice parameters, number densities of unit cells and smallest allowed wavelength of phonons for sodiu cobalt oxide (NCO) and calcium cobalt oxide (CCO).

	a [nm]	**b** [nm]	**c** [nm]	$\mathbf{V_{unitcell}}$ [m^3]	**N** [m^{-3}]	$\boldsymbol{\lambda_0}$ [m]
NCO [20]	0,283	0,283	1,095	$9{,}77 * 10^{-29}$	$1{,}14 * 10^{28}$	$7{,}16 * 10^{-10}$
CCO [6]	0,483	0,282	1,085	$1{,}48 * 10^{-28}$	$6{,}77 * 10^{27}$	$8{,}52 * 10^{-10}$
CCO [6]	0,483	0,455	1,085	$2{,}38 * 10^{-28}$	$4{,}19 * 10^{27}$	$9{,}99 * 10^{-10}$

literature. There are two different velocities of sound in solids corresponding to longitudinal waves ($v_{s,l}$ see Equation 7) and shear waves ($v_{s,s}$ see Equation 8). They are derived from mechanical properties with the following equations [21] and given in Table 3 below.

$$v_{s,l} = \sqrt{\frac{K + \frac{4}{3}G}{\rho}} = \sqrt{\frac{Y\,(1-\nu)}{\rho\,(1+\nu)\,(1-2\nu)}} \tag{7}$$

$$v_{s,s} = \sqrt{\frac{G}{\rho}} \tag{8}$$

K = bulk modulus, G = Shear modulus Y = Young's modulus, ν = Poisson's ratio and ρ = density

Table 3: Mechanical properties and velocities of sound for sodium cobalt oxide and calcium cobalt oxide.

	K [GPa]	**G** [GPa]	$\boldsymbol{\rho}$ [$\frac{kg}{m^3}$]	**Y** [GPa]	$\boldsymbol{\nu}$ [-]	$\mathbf{v_{s,l}}$ [$\frac{m}{s}$]	$\mathbf{v_{s,s}}$ [$\frac{m}{s}$]
NCO [22, Ch. 44]	33,68	19,9	3640	49,8	0,25	4057	2338
CCO [23]	21,58	13,3	3220	33,1	0,24	3494	2032

The resulting Debye temperatures for both materials and both types of phonon waves are given in the following table (Table 4). They are also calculated for both different unit cells of CCO.

Table 4: Calculated Debye temperatures for all cases.

	$\mathbf{T_{0,l}}$ [K]	$\mathbf{T_{0,s}}$ [K]
NCO	272,15	156,84
CCO(b=0,282)	196,97	114,57
CCO(b=0,455)	167,94	97,68

All Debye temperatures are below 0°C and therefore constant ratios for $\frac{\lambda_\alpha}{\lambda_0}$ are applicable. These ratios are given in [1, Ch. 42] and the ones weighted

by thermal conductivity and modeled by Debye dispersion are used. This results in the wavelengths given in Table 5.

Table 5: Calculated values of λ_{10} and λ_{90}.

	$\boldsymbol{\lambda_0}$ [nm]	$\boldsymbol{\lambda_{10}}$ [nm]	$\boldsymbol{\lambda_{90}}$ [nm]
NCO	0,72	0,74	1,54
CCO (b=0,282)	0,85	0,89	1,83
CCO (b=0,455)	0,99	1,04	2,15

3.2 Phonon wavelengths obtained from Raman spectroscopy

If atoms are exited by photons to a virtual energy state they can emit slightly lower (Stokes scattering) or slightly higher (Anti-Stokes scattering) energy. This energy is stored in or taken from optical phonons. The Raman shift $\Delta\omega$ (difference between excitation wavenumber and returning wavenumber) can be used to recalculate the measured wavelength λ_1 (Equation 9) and this is needed to calculate the wavelength of the excited phonon λ_{ph} (Equation 10).

$$\Delta\omega = (1/\lambda_0 - 1/\lambda_1) \tag{9}$$

$$\lambda_{ph} = \lambda_1 - \lambda_0 \tag{10}$$

Several Raman shifts from literature and the corresponding phonon wavelengths are given for both substances in the following table (Table 6).

Table 6: Raman shifts $\Delta\omega$, and wavelengths for sodium cobalt oxide and calcium cobalt oxide from literature.

	$\boldsymbol{\Delta\omega}$ [cm^{-1}]	$\boldsymbol{\lambda_0}$ [nm]	$\boldsymbol{\lambda_1}$ [nm]	$\boldsymbol{\lambda_{ph}}$ [nm]
NCO [24]	415	514.5	525.73	11.23
	430	514.5	526.14	11.64
	460	514.5	526.97	12.47
	497	514.5	528.00	13.50
	576	514.5	530.21	15.71
CCO [25]	180	514.5	519.31	4.81
	300	514.5	522.57	8.07
	358	514.5	524.15	9.65
	440	514.5	526.42	11.92
	545	514.5	529.34	14.84
	568	514.5	529.99	15.49
	630	514.5	531.74	17.24
	660	514.5	532.58	18.08
	685	514.5	533.30	18.80

3.3 Mean-free path of phonons

Besides the wavelengths the mean-free path of phonons (Λ) is another characteristic property of them. It can be calculated via Equation 11 with κ the thermal conductivity and the specific heat C [1, Ch. 42], if information on these bulk properties is available.

$$\Lambda = \frac{3\kappa}{v_s C} \tag{11}$$

However this bulk mean-free path of phonons is just a simplification and the actual range of mean-free paths can differ significantly [1, Ch. 42]. In a similar cutoff approach as in subsection 3.1 is bared that the ratio $\Lambda_{90}/\Lambda_{10}$ can happen to be up to several hundreds [26]. The mean-free path of phonons seems to be easier affected by superlattice periods than the wavelengths[1, Ch. 42], because of the dimensions of single layer thicknesses. This is especially the case for thermal transport perpendicular to the layers.

3.4 Conclusion theoretical part

The wavelengths of phonons responsible for 80% of the thermal conduction by the lattice are in both materials in the range between approximately 1 and 2 times the thickness of a single layer of the used materials (see Table 5). In comparison silicon has a similar number density of unit cells (approximately $6.24{\cdot}10^{27}$ m^{-3} with dimensions of unit cell taken from webelements.com), but a lot higher velocity of sound (7510 m/s [27]). This results in a higher Debye temperature and therefore the used constant values for λ_α/λ_0 are not applicable, but Equation 6 instead, which gives higher values for all cutoff-wavelengths [1, Ch. 42]. Roughness and mixing effects at the layer interfaces seem to have much influence on the phonon scattering, because they appear in the same wavelengths. Superlattices consisting of alternating single layers or varying layers of 1 or 2 single layers are expected to have much poorer properties (e.g. resistivity) and are not possible to grow at sufficient precision. From earlier research is evident, that the properties of thin films get significantly poorer at layer thicknesses lower than 10 nm. Therefore is this the starting point for superlattices in the practical part of this work, although smaller layers should have more effect on the thermal conductivity.

Wavelengths of optical phonons obtained from Raman spectroscopy are situated for Na_xCoO_2 between 11 nm and 16 nm and for $Ca_3Co_4O_9$ between 5 nm and 19 nm. Superlattices with layer thicknesses in this order are much easier to built than the earlier calculated range. However optical phonons tend to carry less heat than acoustical phonons [28]. Therefore the effects of scattering these phonons can be as small, as estimated by the cutoff formula (<10%) and are not very promising.

4 Practical aspects

4.1 Sample fabrication

4.1.1 Pulsed laser deposition

For PLD a custom-built standard setup is used that is provided by TSST BV. It consists of a high vacuum chamber with load-lock. The used excimer laser is the LPX 200 by *Lambda Physik*. The parameters used for all depositions are given in Table 7. The target used for the deposition of the Na_xCoO_2 phase has the composition $Na_{0.9}CoO_2$, because of the volatility of the Na atoms. The given deposition temperature is the temperature setpoint of a thermocouple attached inside the heater, so that the temperature at the surface of the substrate can slightly differ. In earlier research is found that sodium cobalt oxide can be grown well crystalline at the used temperature. Calcium cobalt oxide would grow better at higher temperatures [29], but the temperature is kept constant to prevent the loss of volatile sodium atoms out of the deposited layers. To get saturated oxides all depositions are carried out in a pure oxygen environment. The laser repetition rate is kept quite low to give the deposited layers sufficient time for crystallographic ordering and oxygen saturation.

Table 7: Used parameters for depositions.

Deposition temperature (T_{dep})	430 °C
Deposition pressure (p_{dep})	0.4 mbar
Laser fluence	4 J/cm^2
Spot size	1.08 mm^2
Target-to-substrate distance	55 mm
Repetition rate	1 Hz

All produced samples are grown on LSAT substrates and can be seen in Table 8. At first reference samples are prepared from both substances to be able to compare the measurements of the superlattices later on. Because pure $Ca_3Co_4O_9$ grows not crystalline at all under these deposition conditions, it was grown again on top of a 10 nm Na_xCoO_2 layer. As earlier mentioned are Na_xCoO_2 thin films not stable if exposed to air. Therefore are all samples containing Na_xCoO_2 provided with an AlO_x capping layer (approximately 50 to 80 nm). This amorphous layer should have no influence on the measurements. The substrates are attached to the heater with silver glue.

Table 8: Produced samples.

Sample	Denotation	Thickness	Capping layer
Reference Na_xCoO_2	NCO	200 nm	✓
Reference $Ca_3Co_4O_9$	CCO	110 nm	
10 nm NCO/10 nm CCO	SL(10/10)	200 nm	✓
5 nm NCO/10 nm CCO	SL(5/10)	150 nm	✓
10 nm NCO/5 nm CCO	SL(10/5)	150 nm	✓

4.1.2 Preparation for measurements

To allow easy electrical measurements (see subsection 4.2) all samples are provided with sputtered gold contacts at all four corners. In the case of the reference sample of CCO these contacts are just added onto the surface by using a mask that is covering the rest of the sample. A slight amount of titanium is added between the sample and the gold contact to ensure a better attachment. The AlO_x capping layer on top of the NCO reference sample has to be removed at first by means of etching before the gold contacts are added in the same manner. To maintain the rest of the capping layer the same mask is used for etching and gold sputtering. The superlattice samples are treated in the same way, but with a different etching time. To make good contact with the whole superlattice structure all layers are removed at the corners and afterwards the amount of gold sputtered is adjusted to ensure that the gaps are refilled completely at least. Because the used two dimensional mask is covering only the top surface of the samples the edges have to be cleaned afterwards manually to ensure that there is no direct connection between the contacts by gold. Also possible residues of the silver glue used by PLD are removed at the edges this way. This cleaning step can be crucial as explained later on in subsection 5.3. All etching is done with a custom-made sputter etching setup using argon. Sputtering is done in an *Perkin-Elmer Ultek vacuum system.*

4.2 Measurement

4.2.1 X-ray diffraction

With an x-ray diffraction (XRD) setup $2\theta/\omega$ scans are done of the samples. In this scan the sample is kept constant and an x-ray beam is spotted onto the middle of it. Now the angle of the x-ray source is varied and the detector is adjusted in the same way that the detector-sample angle ω matches the source sample angle θ. It is called a 2θ scan, because this is the angle between the incoming x-ray beam and the diffracted x-ray beam. The type of diffraction is called Bragg reflection and the interplanar distance d in

the material can be determined by the peak positions via Bragg's law (see Equation 12) [30]. λ is the wavelength of the used x-ray beam and n the order of the peak. All scans are done with a *PANalytical X'Pert Pro* diffractometer and the parameters given in Table 9.

$$n\lambda = 2d \sin\theta \tag{12}$$

Table 9: Used parameters for XRD scans.

X-ray type	Cu $K_{\alpha 1}$
Wavelength λ	0.154 nm
Mirror type	W/Si, parabolic
Monochromator type	Ge (220), asymmetric
Divergence slit	1/16"
Distance slit to sample	220 mm
Detector	*PIXcel 3D*

4.2.2 Seebeck measurement

The experimental setup that is used to determine the Seebeck coefficient of the samples at ambient conditions is schematically given in Figure 1. It makes use of 2 Peltier elements and 2 thermocouples. The sample is positioned on top of the two Peltier elements so that one edge is cooled by the first Peltier element and the other edge is heated by the second Peltier element if a current is applied through the Peltier elements. A *Keithley* 6221 current source as well as 3 *HP* 34401A multimeters are used.

One junction of each thermocouple is held inside a cold reservoir with a mixture of ice and water to maintain a constant temperature of 0°C. The other two junctions of the thermocouples are attached to contacts of the sample at both sides. The used thermocouples are of the commercial type K. The type K thermocouples consist of alumel and chromel two nickel alloys. The voltage of each thermocouple corresponds to the temperature at the respective side of the sample. Furthermore the voltage difference between two respective wires of the thermocouples can be used to calculate the Seebeck voltage. Therefore it is measured with a third multimeter. The measured Voltage is the sum of the Seebeck voltage that arises inside the sample and the Seebeck voltage that arises inside the wires made of alumel due to the temperature difference.

With this setup it is possible to measure the temperatures of the sample edges and the Seebeck voltage at the same time and place. With *LabVIEW* automatically a constant current is applied and then 10 voltage measurements are carried out after a time of 45 seconds to let the temperature get

Figure 1: Schematic setup for Seebeck measurements at room temperature.

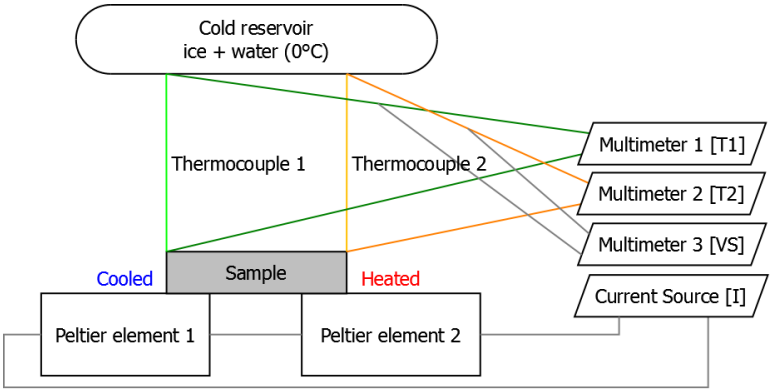

stable. Several different currents are measured and the observed Seebeck voltages are plotted against the temperature difference. The slope of the linear least-square fit is the total Seebeck coefficient and afterwards it is corrected for the Seebeck coefficient of the alumel wiring ($18.5\mu V/K$) [31].

4.2.3 Resistivity measurement

To measure the resistivity of the samples the van der Pauw technique [32] is used. This technique allows measuring the sheet resistivity ρ_s of the sample. The rectangular flat sample is connected via 4 gold contacts at the corners. Using a 4-probe method instead of 2 probes neglects the effects of the wiring and the contacts [1, Ch. 23]. It is necessary that the contacts are placed at the outer edges of the sample and not inside [1, Ch. 23]. A current is led through two adjacent contacts and the other two are used to determine the resistance by measuring the voltage (see Equation 13). A second resistance in the other direction of the sample is measured by rotating the contact configuration by 90°. From these 2 directional resistances the sheet resistance ρ_s can be obtained by numerical solving of the van der Pauw formula (Equation 14). To obtain the average resistivity the sheet resistance has to be multiplied by the layer thickness d (Equation 15). The measurements are done with a *HP* 34401A multimeter.

$$R_{12,34} = \frac{U_{34}}{I_{12}} \tag{13}$$

$$e^{-\pi \frac{R_{12,34}}{\rho_s}} + e^{-\pi \frac{R_{23,41}}{\rho_s}} = 1 \tag{14}$$

$$\rho = \rho_s d \tag{15}$$

5 Results and discussion

5.1 X-ray diffraction

Two different $2\theta/\omega$ XRD-scans are done for each sample. The first scan was a broad scan ranging from 10° to 110° to detect all peaks. It is exemplary given for NCO in Figure 2. The four peaks expected for the substrate are indicated in this figure, too, and represent from left to right the vectors 001, 002, 003 and 004. The 002 substrate peak is used for alignment, because it is quite high and sharp. The other four peaks that are visible result from the thin film. The first peak around 16° is the most significant and therefore used for detailed comparison of all samples (see Figure 3). Because a sample consisting of solely a calcium cobalt oxide 200 nm thin film on LSAT showed no other peaks, besides the ones arising from the substrate it is replaced by the earlier mentioned CCO reference sample. That indicates that sole calcium cobalt oxide tends not to grow crystalline on LSAT at all under the present deposition conditions.

Figure 2: $2\theta/\omega$ XRD scan of the NCO sample with logarithmic scale ranging from 10° to 110°. The substrate LSAT peaks are indicated.

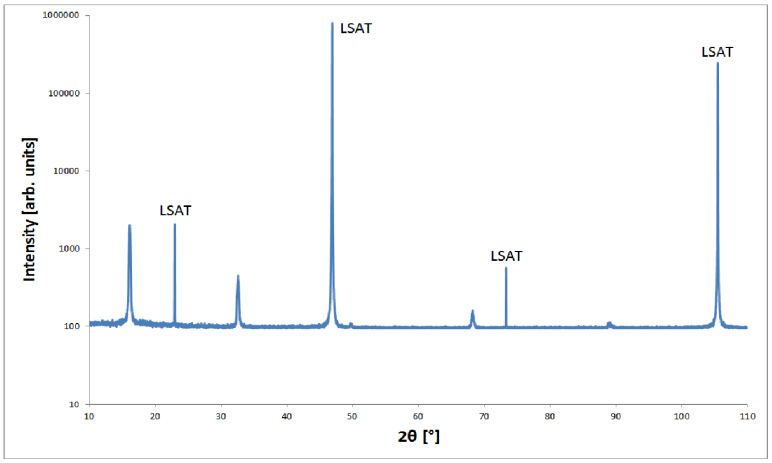

Figure 3 shows the peaks around 16° in the detailed $2\theta/\omega$ XRD scans. Concerning the height and form of the peaks can be concluded that the NCO sample is the most crystalline one and the CCO sample the lowest. This was expected, because $Ca_3Co_4O_9$ was not crystalline at all under the used deposition parameters before it was added on top of a thin Na_xCoO_2 layer. This suggests that Na_xCoO_2 has an ordering effect on $Ca_3Co_4O_9$ due to the similar lattice structure and the fact that sodium cobalt oxide grows well crystalline. The SL5/10 sample has only little amount of Na_xCoO_2 compared to $Ca_3Co_4O_9$ and therefore is just slightly more crystalline than CCO. In similar manner one would expect that the SL10/10 sample is less crystalline than the SL10/5 sample, but it seems the other way round.

Figure 3: Detailed $2\theta/\omega$ XRD scan between 12° and 20° with logarithmic scale. A noise level correction is applied for comparison. Samples: NCO - dark blue, SL10/5 - green, SL10/10 - red, SL5/10 - light blue, CCO - purple.

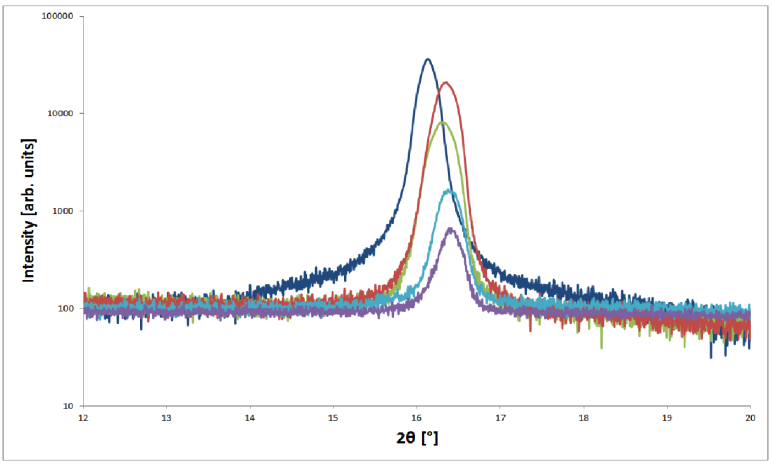

The peak of the NCO sample is positioned at approximately 16.13°. Using Bragg's law (Equation 12) this corresponds to a distance between the lattice points of 10.98 Å which is according to literature comparable to the length of the c axis of Na_xCoO_2 with sodium contents x of slightly below 0.5 [5, 20]. The CCO peak (16.39°) results in an inter planar distance of 10.8 Å, which also is comparable to literature values for the c-axis of $Ca_3Co_4O_9$ [6]. The CCO peak seems to be asymmetrical which is the influence of the small Na_xCoO_2 layer on the substrate. The peak positions and lattice spacings for the superlattices can be seen in Table 10.

Table 10: XRD peak positions and calculated inter planar distances.

Sample	Peak position	Inter planar distance
NCO	16.13°	10.98 Å
SL10/5	16.3°	10.86 Å
SL10/10	16.36°	10.82 Å
SL5/10	16.38°	10.81 Å
CCO	16.39°	10.8 Å

There are two possible scenarios for the superlattice samples. First scenario is, that both phases grow independently and two peaks arise, that may overlap due to the scan conditions. The second scenario is that both layers affect each other and one of them or both will be stretched out or compressed. All superlattice peaks are single peaks without observable asymmetry. The positions of the peaks are given in Table 10 and are increasing with the CCO:NCO ratio. Furthermore the SL10/10 with the same amount of layers of both materials is not located exact in the middle of the two reference

peaks, but shifted towards the CCO peak. This shift can be explained by the larger amount of atoms in the CCO layer which is resulting in a larger number of reflections. It can not be concluded which of the mentioned scenarios is the most applicable. Maybe it is possible to decide in a scan with higher resolution if there are two different peaks or not. Also some mixed layers are possible arising due to sodium or calcium diffusion, but not expected to have much influence.

5.2 Seebeck coefficient

The measured average Seebeck coefficients are given in Figure 4 with the standard deviation of the measurements at all four edges of the samples. The Seebeck coefficient of the NCO sample is 79 $\pm$ 3 $\mu V/K$, which is slightly higher than other reported values of thin films and comparable to single crystal values (compare Table 1). By the CCO sample is an average Seebeck coefficient of 136 $\pm$ 7 $\mu V/K$ measured. This value is lower than reported Seebeck coefficients. This can be due to the poor crystal growth at the present deposition conditions. The earlier mentioned sample of a pure thin film of $Ca_3Co_4O_9$ had an even smaller Seebeck coefficient of approximately 81 $\mu V/K$.

Figure 4: Measured Seebeck coefficients plotted with standard deviations. The samples are ordered by increasing CCO:NCO ratio.

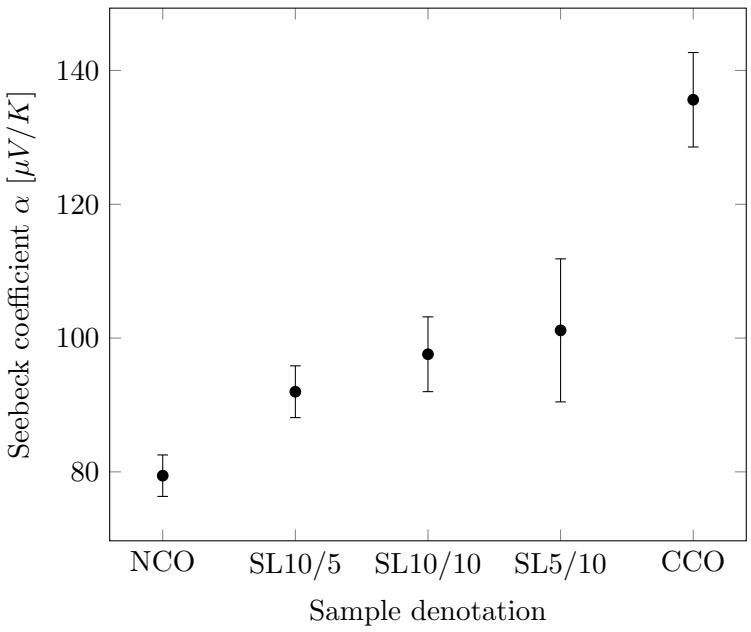

The superlattice samples are positioned in between those two values and the Seebeck coefficient is monotonically increasing with the CCO:NCO ratio.

This indicates that the superlattice structure does not affect the Seebeck coefficient significantly and a *mixed* value of both phases is measured. The SL(5/10) sample has a higher standard deviation than the other samples, even after doing extra measurements. This can be due to a heterogeneity in the sample leading to significantly different Seebeck coefficients at different edges of the sample (up to 30 $\mu V/K$ difference). Another evidence for this is the fact that the XRD peak of this sample was the smaller compared to the other superlattices.

5.3 Resistivity

The measured resistivity of the NCO reference sample is 1.45 mΩcm. This value is comparable to literature values for thin films grown on other substrates mentioned earlier (compare Table 1: 0.8 mΩcm on Al_2O_3 and 1 mΩcm on $LaAlO_3$ [17]). The stability issues mentioned earlier [16] are prevented by an AlO_x-capping layer [17]. However all superlattice samples and the CCO reference sample have no stable resistivity as can be seen in Figure 6. All samples have a capping layer[d] and the rise in resistivity is much smaller than the reported instability of NCO without capping layer [17], but still significant. The resistivities are measured over a time period up to 3 weeks and Figure 6 implies that stability is maybe reached within a period of months to years.

Figure 5: Change in color of the samples. Shown is the sample SL(5/10) on graph paper.

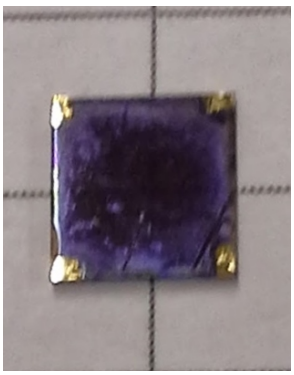

The instability of thin films of Na_xCoO_2 was reported to appear due to a reaction of the volatile sodium with components of the air [17]. Air contact at the top of the samples is prevented by the AlO_x capping layer, but it is still possible via the edges of the samples. In addition there was a change in color arising from the edges slowly heading towards the center, which also suggests a chemical reaction occurring (see Figure 5 on the right). The access of air from the edges was also the case for the stable thin film samples of NCO (this work or in [17]). Either there is a new undiscovered reaction occurring between the two materials or components of the $Ca_3Co_4O_9$ layers work as a catalyst for the earlier found reactions. It is not obvious from this work and may be analyzed by finding a possibility to produce the samples without cleaning the edges or cover them afterwards from air.

[d] besides the CCO reference sample, where the high amount of CCO on top of the small NCO layer was considered to be sufficient

The resistivity plot of the CCO reference sample (6(d)) shows the most asymptotic behavior, which indicates that it may get stable first. This implies that Na_xCoO_2 is the reactive phase, since the CCO sample has significant less content of NCO than the other ones. The this way observed resistivities are not essential and contain not much significant information, because the rising speed of the curves seems arbitrary and the measurements have no clearly defined beginning or end time. Nevertheless it is obvious that the first data points of the superlattices are quite low, which is surprisingly, because previous a significant rise in resistivity was reported for thin layers, as the thickness is lowered [29].

Figure 6: Resistivity plotted against time for all instable samples.

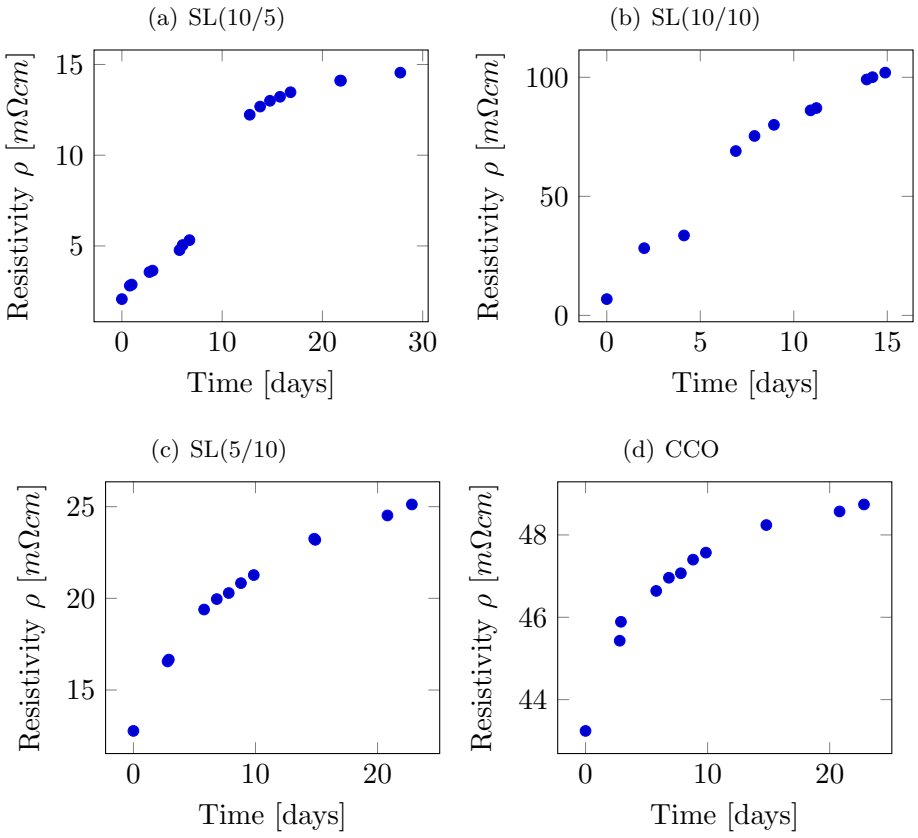

6 Conclusion

Purpose of this study was to research possible enhancement of thermoelectric properties in superlattices of Na_xCoO_2 and $Ca_3Co_4O_9$. This is done by practical measurements of the electric and theoretical considerations of the thermal properties. The most improvement was expected to appear because of a lowering of the thermal conductivity.

XRD measurements showed crystallinity in all used samples. Even $Ca_3Co_4O_9$ grew crystalline under the present deposition conditions after it was added on top of a thin layer of Na_xCoO_2. Furthermore the measured Seebeck coefficients of the grown superlattices were in between the values of both single phases, which indicates that they are not affected by the superlattice structure, but show a *mixed* Seebeck coefficient.

When measuring the resistivity, it appeared that all samples containing both materials were not stable under ambient conditions, but instead the resistivity kept on rising. This behavior was similar to the instability of Na_xCoO_2 thin films discussed earlier, but in contrast it could not be prevented by adding an AlO_x capping layer. The resistivity was a crucial element in this approach, because earlier results [29] showed that it rises in $Ca_3Co_4O_9$ thin films with decreasing layer thickness. A much higher resistivity would lower the ZT and make the superlattice approach unfavorable. However it was a good result, if stable values for resistivities ranging in the same dimensions as the first measurements of the superlattices could be achieved.

The instability of the electric resistivities in the superlattices is the most important aspect for future research. It is still possible, that the instability occurs due to a reaction with components of the air entering the samples from the edges that can be prevented easily. I would suggest measuring samples stored under vacuum conditions or in an inert atmosphere for an amount of time to be clear. If this is the reason for the instability, simply a better practical solution needs to be found to prevent the superlattices from air contact. Another possibility is that the added AlO_x capping layer is not sufficient for superlattices that tend to have more roughness on top than thin layers. This can be tested by increasing the amount of AlO_x.

The theoretical considerations about the thermal conductivity showed, that it is likely to have an effect on thermal transport by phonons along the planes due to impurities and imperfections at the superlattice interfaces, because the wavelengths of the phonons have a similar dimension as the unit cells. It is proposed that the effect on phonons increases with decreasing layer thickness. The obtained Seebeck effects and the first measured resistivities of the superlattices suggest that it is possible to make superlattice with even lower

layer thicknesses that do not show the high resistivities as reported for thin films in this thickness. To especially lower thermal conductivity perpendicular to the crystal planes, it is proposed to make superlattices with lattice periods in the range of the mean-free paths of phonons. However there is more information needed to determine their dimensions.

Acknowledgment

I would like to thank Mark Huijben and Peter Brinks for their general guidance in the course of this project. Especially the practical help, the sample fabrication as well as the provision of earlier obtained results by Peter Brinks allowed me to achieve sufficient understanding of the topic and need to be mentioned.

My special thanks are extended to the whole IMS group for providing an inspiring and motivating atmosphere accompanying the end of my bachelor program and my time at the University of Twente.

References

[1] D.M. Rowe. *Thermoelectrics handbook: macro to nano*. CRC Press, 2006. ISBN: 0849322642.

[2] T.M. Tritt. Thermoelectric materials: Principles, structure, properties, and applications. *Encyclopedia of Materials: Science and Technology (Second Edition)*, 2002. doi:10.1016/B0-08-043152-6/01822-2.

[3] I. Terasaki, Y. Sasago, and K. Uchinokura. Large thermoelectric power in $NaCo_2O_4$ single crystals. *Physical Review B*, 56(20):12685–12687, 1997. doi:10.1103/PhysRevB.56.R12685.

[4] K. Fujita, T. Mochida, and K. Nakamura. High-temperature thermoelectric properties of $Na_xCoO_{2-\delta}$ single crystals. *Japanese Journal of Applied Physics, Part 1: Regular Papers and Short Notes and Review Papers*, 40(7):4644–4647, 2001. doi:10.1143/JJAP.40.4644.

[5] L. Cui, Y.G. Zhao, G.M. Zhang, W.Y. Zhang, Z.P. Guo, W. Ren, X.P. Zhang, and M.H. Zhu. Structural and electronic transport properties of Na_xCoO_2. *Journal of Alloys and Compounds*, 426(1-2):72–75, 2006. doi:10.1016/j.jallcom.2006.03.091.

[6] Y. Miyazaki, M. Onoda, T. Oku, M. Kikuchi, Y. Ishii, Y. Ono, Y. Morii, and T. Kajitani. Modulated structure of the thermoelectric compound $[Ca_2CoO_3]_{0.62}CoO_2$. *Journal of the Physical Society of Japan*, 71(2):491–497, 2002. doi:10.1143/JPSJ.71.491.

[7] M. Shikano and R. Funahashi. Electrical and thermal properties of single-crystalline $[Ca_2CoO_3]_{0.7}CoO_2$ with a $Ca_3Co_4O_9$ structure. *Applied Physics Letters*, 82(12):1851–1853, 2003. doi:10.1063/1.1562337.

[8] Y. Zhang, J. Zhang, and Q. Lu. Rapid synthesis of $Ca_2Co_2O_5$ textured ceramics by coprecipitation method and spark plasma sintering. *Journal of Alloys and Compounds*, 399(1-2):64–68, 2005. doi:10.1016/j.jallcom.2005.02.053.

[9] Y. Huang, B. Zhao, J. Fang, R. Ang, and Y. Sun. Tunning of microstructure and thermoelectric properties of $Ca_3Co_4O_9$ ceramics by high-magnetic-field sintering. *Journal of Applied Physics*, 110(12):123713, 2011. doi:10.1063/1.3671403.

[10] R. Venkatasubramanian, E. Siivola, T. Colpitts, and B. O'Quinn. Thin-film thermoelectric devices with high room-temperature figures of merit. *Nature*, 413(6856):597–602, 2001. doi:10.1038/35098012.

[11] M.V. Simkin and G.D. Mahan. Minimum thermal conductivity of superlattices. *Physical Review Letters*, 84(5):927–930, 2000. doi:10.1103/PhysRevLett.84.927.

[12] S.M. Lee, D.G. Cahill, and R. Venkatasubramanian. Thermal conductivity of $Si - Ge$ superlattices. *Applied Physics Letters*, 70(22):2957–2959, 1997. doi:10.1063/1.118755.

[13] L.D. Hicks and M.S. Dresselhaus. Effect of quantum-well structures on the thermoelectric figure of merit. *Physical Review B*, 47(19):12727–12731, 1993. doi:10.1103/PhysRevB.47.12727.

[14] T.C. Harman, P.J. Taylor, D.L. Spears, and M.P. Walsh. PbTe-based quantum-dot thermoelectric materials with high ZT. In *Eighteenth International Conference on Thermoelectrics, 1999.*, pages 280–284, 1999. doi:10.1109/ict.1999.843386.

[15] G.D. Mahan and L.M. Woods. Multilayer thermionic refrigeration. *Physical Review Letters*, 80(18):4016–4019, 1998. doi:10.1109/ICT.1999.843457.

[16] H. Zhou, X.P. Zhang, B.T. Xie, Y.S. Xiao, C.X. Yang, Y.J. He, and Y.G. Zhao. Fabrication of Na_xCoO_2 thin films by pulsed laser deposition. *Thin Solid Films*, 497(1-2):338–340, 2006. doi:10.1016/j.tsf.2005.10.078.

[17] P. Brinks, H.T. Heijmerikx, T.A. Hendriks, A.J.H.M. Rijnders, and M. Huijben. Achieving chemical stability in thermoelectric Na_xCoO_2 thin films. *RSC advances*, 2(14):6023–6027, 2012. doi:10.1039/c2ra20734f.

[18] T. Sun, J. Ma, Q.Y. Yan, Y.Z. Huang, J.L. Wang, and H.H. Hng. Influence of pulsed laser deposition rate on the microstructure and thermoelectric properties of $Ca_3Co_4O_9$ thin films. *Journal of Crystal Growth*, 311(16):4123–4128, 2009. doi:10.1007/s11664-010-1261-x.

[19] Q. Qiao, A. Gulec, T. Paulauskas, S. Kolesnik, B. Dabrowski, M. Ozdemir, C. Boyraz, D. Mazumdar, A. Gupta, and R.F. Klie. Effect of substrate on the atomic structure and physical properties of thermoelectric $Ca_3Co_4O_9$ thin films. *Journal of Physics: Condensed Matter*, 23(30):305005, 2011. doi:10.1088/0953-8984/23/30/305005.

[20] P. Liu, G. Chen, Y. Cui, H. Zhang, F. Xiao, L. Wang, and H Nakano. High temperature electrical conductivity and thermoelectric power of Na_xCoO_2. *Solid State Ionics*, 179(39):2308–2312, 2008. doi:10.1016/j.ssi.2008.08.010.

[21] L.E. Kinsler, A.R. Frey, A.B. Coppens, and J.V. Sanders. *Fundamentals of Acoustics*. John Wiley and Sons Inc., 4th edition edition, 2000. ISBN: 0471847895.

[22] I. Al-Suraihy, A. Doghmane, and Z. Hadjoub. *Investigation of Ag Doping Effects on $Na_{1.5}Co_2O_4$ Elastic Parameters*. Springer Netherlands, 2009. doi:10.1007/978-90-481-2669-9_44.

[23] S. Pinitsoontorn, N. Lerssongkram, A. Harnwunggmoung, K. Kurosaki, and S. Yamanaka. Synthesis, mechanical and magnetic properties of transition metals-doped $Ca_3Co_{3.8}M_{0.2}O_9$. *Journal of Alloys and Compounds*, 503(2):431–435, 2010. doi:10.1016/j.jallcom.2010.05.027.

[24] J.F. Qu, W. Wang, Y. Chen, G. Li, and X.G. Li. Raman spectra study on nonstoichiometric compound Na_xCoO_2. *Physical Review B*, 73(9):092518, 2006. doi:10.1103/PhysRevB.73.092518.

[25] M. An, S.K. Yuan, Y. Wu, Q.M. Zhang, X.G. Luo, and X.H. Chen. Raman spectra of a misfit layered $Ca_3Co_4O_9$ single crystal. *Physical Review B*, 76(2):024305, 2007. doi:10.1103/PhysRevB.76.024305.

[26] F. Yang and C. Dames. Mean free path spectra as a tool to understand thermal conductivity in bulk and nanostructures. *Phys. Rev. B*, 87(3):035437, 2013. doi:10.1103/PhysRevB.87.035437.

[27] B.L. Zink, R. Pietri, and F. Hellman. Thermal conductivity and specific heat of thin-film amorphous silicon. *Phys. Rev. Lett.*, 96(5):055902, 2006. doi:10.1103/PhysRevLett.96.055902.

[28] P. Pichanusakorn and P. Bandaru. Nanostructured thermoelectrics. *Materials Science and Engineering R*, 67(2-4):19–63, 2010. doi:10.1016/j.mser.2009.10.001.

[29] M. Ihns. Structural engineering of $Ca_3Co_4O_9$ thermoelectric thin films. 2013. Master Thesis. URL: http://essay.utwente.nl/63574/.

[30] R.J.D. Tilley. *Understanding Solids - The Science of Materials*. John Wiley and Sons LTD, 2004. ISBN: 0470852763.

[31] W. Gee and M. Green. An improved hot-probe apparatus for the measurement of seebeck coefficient. *Journal of Physics E: Scientific Instruments*, 3:135–136, 1970. doi:10.1088/0022-3735/3/2/312.

[32] L.J. Van der Pauw. A method of measuring the resistivity and hall coefficient on lamellae of arbitrary shape. *Philips Research Reports*, 13(1), 1958. ISSN: 0031-7918. URL: http://electron.mit.edu/~gsteele/vanderpauw/vanderpauw.pdf.

List of Figures

List of Tables

List of Symbols

Symbol	Description	Unit
α	Seebeck coefficient	[μV/K]
γ	Weighting parameter	[nm K]
θ	XRD incident angle	[°]
Λ	Mean-free path	[nm]
λ	Wavelength	[nm]
κ	Thermal conductivity	[W/m·K]
ν	Poisson's ratio	[-]
ρ^{e}	Resistivity	[mΩ·cm]
ρ_s	Sheet resistance	[Ω/sq.]
Φ	Efficiency	[-]
$\Delta\omega$	Raman shift	[cm^{-1}]
C	Specific heat	[J/m^3·K]
d	Distance	[nm]
e	Euler's number	[-]
G	Shear modulus	[GPa]
h	Planck's constant	
I	Electric current	[A]
K	Bulk modulus	[GPa]
k_B	Boltzmann's constant	
N	Number density of unit cells	[m^{-3}]
n	Integer	[-]
PF	Power Factor	[μW/K^2·cm]
R	Electrical resistance	[Ω]
T	Temperature	[K]
U	Voltage	[V]
V	Volume	[m^3]
v_s	Velocity of sound	[m/s]
Y	Young's modulus	[GPa]
ZT	Dimensionless figure-of-merit	[-]

[e] In Equation 7, Equation 8 as well as Table 3 ρ corresponds to mass density [kg/m^3]